THERMOELECTRIC CHARACTERISTICS OF RARE-EARTH COPPER CHALCOGENIDES

SYNTHESIS AND INVESTIGATING THERMOELECTRIC CHARACTERISTICS OF THE RECuQ_2 (RE= Pr, Sm, Gd, Dy, Er AND Q= Se, Te)

BY

MEHDI ESMAEILI, M.Sc.

A Thesis
Submitted to the School of Graduate Studies
in Partial Fulfillment of the Requirements
for the Degree
Master of Science

McMaster University

MASTER OF SCIENCE (2014) McMaster University

Department of Chemistry and Chemical Biology Hamilton, Ontario

TITLE: Synthesis and investigating thermoelectric characteristics of the $RE\mathrm{Cu}Q_2$ (RE= Pr, Sm, Gd, Dy, Er and Q= Se, Te)

AUTHOUR: Mehdi Esmaeili, M.Sc. (McMaster University)

SUPERVISOR: Professor Yurij Mozharivskyj

NUMBER OF PAGES: v, 42

Table of Contents

1. Abstract 3

2. Introduction 5

  2.1. Thermoelectric efficiency 7

  2.2. Seebeck coefficient 9

  2.3. Electrical conductivity 9

  2.4. Thermal conductivity 10

  2.5. Optimal materials for thermoelectricity 11

  2.6. Skutterudites 11

  2.7. Clathrates 12

  2.8. Chalcogenides 12

3. Experimental section 14

  3.1. Synthesis methods 14

  3.2. Analysis methods 15

    3.2.1. Powder X-ray diffraction 15

    3.2.2. Single crystal X-ray diffraction 18

    3.2.3. Energy dispersive X-ray spectroscopy (EDS) 22

    3.2.4. Differential thermal and gravimetrical analyses (DTA and TGA) 22

    3.2.5. Physical properties measurement 24

    3.2.6. Electronic structure calculations 24

4. Results and discussion 25

  4.1. Crystal structure 25

    4.1.1. *RE*CuSe_2 25

    4.1.2. *RE*CuTe_2 26

  4.2. Electronic structure 28

    4.2.1. *RE*CuSe_2 28

    4.2.2. *RE*CuTe_2 30

  4.3. Physical properties 31

5. Conclusion and future work 34

6. References 36

1. Abstract

The main focus of this research was to synthesize and then to characterize the potential high-performance thermoelectric materials. In this regard, we have prepared a series of pure *RE*$CuSe_2$ (with *RE* = Pr, Sm, Gd, Dy and Er) and *RE*$CuTe_2$ (with *RE* = Er, Dy and Gd) and analyzed their crystal structure, electronic and physical properties.

We used powder and single crystal X-ray diffraction techniques to analyze their crystal structures and employed energy dispersive X-ray spectrometry (EDS) to verify their chemical compositions. The temperature stability of the synthesized samples was examined by differential thermal and gravimetrical analysis. The high-purity consolidated pellets were prepared for physical properties measurements. We analyzed the relationship between their crystal structures and pertinent electronic properties through the LMTO calculations.

The *RE*$CuSe_2$ phases adopt two structures, monoclinic and trigonal. The monoclinic structure ($P2_1/c$, $z = 4$) is observed for lighter rare earths (*RE* = Pr, Sm and Gd) and Cu-disordered trigonal structure for heavier rare earths ($P\overline{3}m1$, $z = 1$, *RE* = Dy and Er). The resistivity and Seebeck coefficient measurements indicate that the studied selenides are *p*-type semiconductors with relatively small activation energies (0.045-0.12 eV). However, their electrical resistivities are too high (0.49-220 Ohm·cm at room temperature) to make them competitive thermoelectric materials. Electronic structure calculations indicate presence of a band gap in the *RE*$CuSe_2$ phases.

The synthesized RECuTe$_2$ phases (RE = Er, Dy and Gd) adopt a monoclinic-distorted variant ($C2/m$, z = 2) of the trigonal structure ($P\bar{3}m1$, Z= 1) observed for the RECuSe$_2$ (with RE = Dy, Er). While such disorder may be beneficial for lowering their thermal conductivity, large values of electrical resistivity (0.02-0.87 Ohm·cm at room temperature) make these phases unsuitable for practical applications. Comparing to the corresponding semiconducting selenides, the tellurides have lower resistivities, and display a metallic type resistivity. Such behavior stems from the closure of band gaps, which is verified by the electronic structures calculations.

Structurally the RECuTe$_2$ phases (with RE = Er, Dy and Gd) are similar to RECuSe$_2$ with the $P\bar{3}m1$ structure. The monoclinic distortion in RECuTe$_2$ is driven by Cu displacement inside the larger tetrahedral voids in the hexagonal close packing of the Te atoms. Most likely, Cu shifts to one side of the Te tetrahedra to optimize the Cu-Te interactions.

2. Introduction

The finite available amounts of fossil fuels and the increasing rate of energy consumption have been led to strong demand for renewable sources of energy such as solar, wind, biofuels, geothermal, hydroelectric, etc. Also large efforts are undertaken to increase efficiency of energy use. In a typical car, less than one-quarter of the fuel energy is used as propulsion and the rest is wasted as heat [1]. In this light, converting even a fraction of waste heat in cars or large industrial processes into usable electricity should significantly reduce the total energy consumption.

Thermoelectric generators are devices that can directly convert waste heat into electricity and this effect is known as the Seebeck effect. Thermoelectric materials can also be operated reversely by using an external current to create a temperature gradient and this effect is known as the Peltier effect. Thermoelectrics offer high reliability and long life time, however their efficiency is relatively low, and as such they find only limited applications (e.g. deep space probes).

Thermoelectric devices consist of two semiconductors, p- and n- type. The schematic of a simplified device is shown in Figure 1 in two modes: power generation (left) and refrigeration mode (right). In both cases there is a temperature gradient along the two types of semiconductors with hot (red) and cold (blue) sides connected to the metals junctions. The metal layers role is to make a circuit in such a way that the two legs be connected in series in terms of the electric current and in parallel for the thermal current.

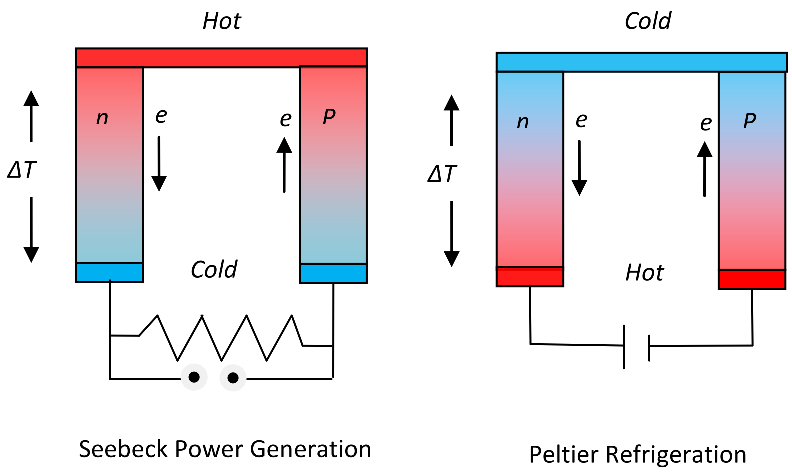

Figure 1. a simplified schematic of using thermoelectrics for power generation and cooling system.

In power generation mode (left) the thermally activated electrons travel from a metal (top) to an n-type semiconductor and to a metal. They produce electrical power across the load and return to a metal (bottom the of p-type semiconductor), to a p-type semiconductor and finally back to a metal (top). In fact, the temperature gradient, ΔT, generates the voltage, V, across the load by the Seebeck effect, α, (equation 1). The produced voltage forces the current to flow through the load.

$$\alpha = \frac{V}{\Delta T} \qquad (1)$$

The effect of temperature gradient in a metal or in a semiconductor can be characterized by the Fermi-Dirac distribution (equation 2). The probability, $f(E,T)$, of finding a fermion (electron) at given energy, *E*, and temperature, *T*, is given by

$$f(E,T) = \frac{1}{e^{\frac{(E-\mu)}{K_B T}} + 1} \qquad (2)$$

where k_B is the Boltzmann constant. According to the above equation, more electrons with higher energies are obtained at high temperatures. Electrons of the higher energy level will diffuse from the hot side to the cold side or to the lower energy state and thus the concentration gradient (and current) is established.

There is a number of applications for thermoelectric materials, e.g. communication instruments in remote locations (i.e. weather, radio and TV relay stations), deep space probes. Thermoelectric materials are preferred where the reliability and absence of moving parts outweigh their cost and efficiency. However, low efficiency and cost of thermoelectric devices are some drawbacks compared to traditional power generators or refrigerators.

2.1. Thermoelectric efficiency

The efficiency of thermoelectric materials is represented by the dimensionless Figure-of-Merit

$$ZT = \frac{\alpha^2 \sigma T}{\kappa} \tag{3}$$

where α is the Seebeck coefficient, σ is the electrical conductivity, κ is the thermal conductivity and T is the absolute temperature [2]. Despite the possibility of having high-efficiency thermoelectric materials, achieving high ZT values is difficult and current ZT values remain between 1 and 2 [3]. The reason is that the three material properties are not completely independent but rather compromise each other (figure 2). For instance, increasing the carrier concentration doesn't necessarily lead to higher

ZT values because it is directly related to the electrical conductivity and electronic part of the thermal conductivity but reversely to the Seebeck coefficient.

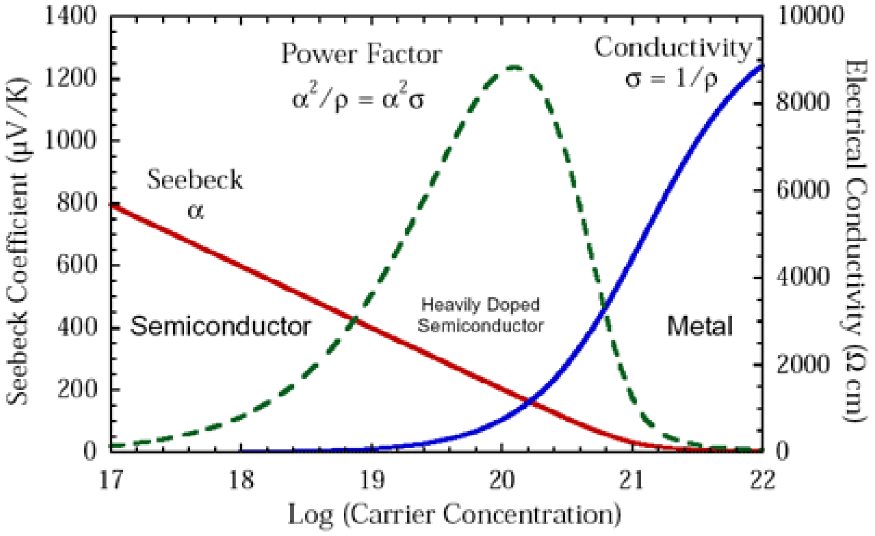

Figure 2. The relationship between seebeck coefficient, electrical conductivity and logarithm of carrier concentration [1]. Heavily doped semiconductors give the optimal power factor for a high efficiency thermoelectric material.

To attain a highly-efficient thermoelectric material, a high power-factor ($\alpha^2\sigma$) and a low thermal conductivity are required. In order to preserve a high electrical conductivity but reduce the lattice thermal conductivity (that is the heat transferred by phonons), Slack proposed a “phonon glass- electron crystal” (PGEC) [2]. Most of the recent progress in the field has been attained due to lowering the thermal conductivity rather than increasing thermopower or power-factor. Some structures such as skutterudites or clathrates with rattling heavy elements, or structures with defects, atomic disorder and superlattices offer low thermal conductivities. A detailed discussion about the thermoelectric parameters will be provided first, and then optimal materials for thermoelectric applications will be analyzed.

2.2. Seebeck coefficient

For metals and degenerate semiconductors, the relationship between the Seebeck coefficient (S) and charge carrier concentrations (n) is described by the equation below [3].

$$S = \frac{8\pi^2 K_B^2}{3eh^2} m^* T \left(\frac{\pi}{3n} \right)^{2/3} \quad , \qquad (4)$$

where e is the charge of an electron, h is the Planck's constant, n is carrier concentration and m^* is the effective mass of carriers. Electrons and holes are charge carriers in a crystal; they behave differently in response to the electric or magnetic field.

2.3. Electrical conductivity

Under the electrical potential difference across a (semi-) conducting crystal, the mobile charge carriers will generate an electrical current. The carrier movement is characterized by electrical conductivity, which is given as [2]:

$$\sigma = ne\mu \qquad (5)$$

where μ is the carrier mobility. The carrier mobility is expressed as the product of the carrier scattering time (τ), i.e. the time during which the carriers lose the momentum, the effective mass (m^*) and the charge of carriers [2].

$$\mu = \frac{e\tau}{m^*} \qquad (6)$$

Electrical conductivity is a function of temperature. In semiconductors, conductivity increases with the temperature due to an increase in the number of charge carriers. The number of charge carriers in semiconductors is exponentially proportional to the band gap size (ΔE) and temperature through the Arrhenius equation.

$$n \propto \exp^{\frac{-Eg}{2KT_B}} \qquad (7)$$

In metals, however, increasing temperature results in a lower conductivity, because phonon vibrations, which increase with temperature, decrease the carrier mobility.

2.4. Thermal conductivity

The thermal conductivity is the result of heat transferred through a material. The heat can be transferred by both the charge carriers and lattice vibrations, i.e. phonons. Therefore, the total thermal conductivity is derived by the sum of both carrier and phonon contributions.

$$\kappa = \kappa_e + \kappa_{Ph} \qquad (8)$$

Accordingly, materials with a large Seebeck coefficient and small κ are favored for approaching high ZT values.

2.5. Optimal materials for thermoelectricity

An optimum material for thermoelectric applications should possess a high Seebeck coefficient, high electrical conductivity and a low thermal conductivity. For commercial applications, some other parameters such as cost, toxicity and availability of constituent elements must be also considered. In this section, I will first review some of the most promising thermoelectric compounds and then will focus on chalcogenides.

2.1. Skutterudites

Skutterudites are binary compounds of the AB_3 composition, in which A stands for a metal like Co, Fe, Rh, Ir and B is a pnictogen like P, As, Sb. Skutterudites have cubic structure (Figure 3), where only six out of the available eight cubes contain planar units of pnictogens. There are two vacant cubes or voids per unit cell in each crystal structure of skutterudites, which are big enough to embed large lanthanide atoms (R), and make a general formula of $R_{(1-x)}A_4B_{12}$ ($x \leq 1$) [4].

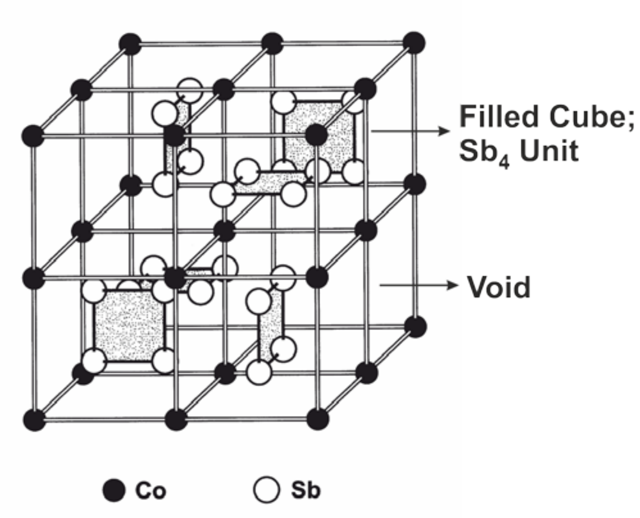

Figure 3. Depiction of an unfilled skutterudite, where A= Co and B= Sb in an AB_3 composition. 6 out of the 8 cubes are occupied by planar Sb_4 units and 2 cubes are left unoccupied. Voids may be, partially or fully, filled by a lanthanide.

Intercalating lanthanides as guest atoms into the skutterudite voids has been resulted in thermoelectric properties with rather high ZT values. The ZT value of $Ce_{0.9}Fe_3CoSb_{12}$ is expected to reach 1.4 at high temperatures [4]. Partial filling of the voids has shown to increase the power factors [5]. However, skutterudites are not the only optimized thermoelectric materials but many other compounds have rendered even higher ZT values.

2.2. Clathrates

Clathrates are typically formed in a cubic structure with an empirical formula of $A_8B_{16}C_{30}$ (A= Sr, Ba, B= Al, Ga and C= Si, Ge). They are known for their cage-type structures, comprised of 20- or 24-atoms [6]. These oversized cages provide a large space for their guest *A* atoms to rattle, which results in very low thermal conductivity. A structure of a narrow band gap semiconducting clathrate $Ba_8Ga_{16}Si_{30}$ is given in Figure 4.

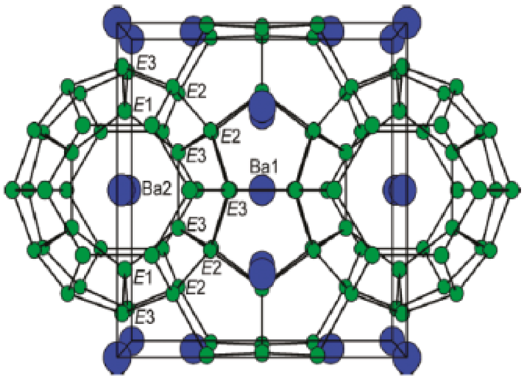

Figure 4. Schematic view of $Ba_8Ga_{16}Si_{30}$ clathrate, E= Ga and Si.

2.3. Chalcogenides

Chalcogenides are the first known thermoelectric materials [7]. The Bi_2Te_3-based materials can be either a p- or n-type semiconductor [7]. The ternary $CsBi_4Te_6$ is a high-performance thermoelectric compound suitable for room-temperature applications [38]. In the layered crystal structure of $CsBi_4Te_6$, Cs^+ cations possess large atomic displacement parameters compared to Bi and Te atoms, which results in a rattling effect and reduced heat transport through the material. The Bi-Bi bonds in this structure render a small band gap, i.e. 0.1 eV, which yield a high ZT value at low temperatures [8].

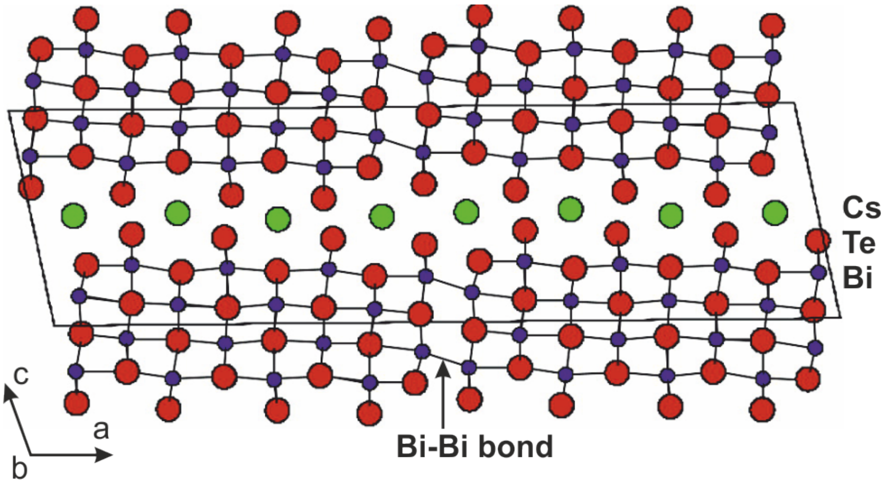

Figure 5. Monoclinic crystal structure of $CsBi_4Te_6$ along the b-axis.

Recently, the β-copper selenide, $Cu_{2-x}Se$ ($x > 0$), has been shown to have a ZT of 1.5 at 1000 K [9]. The origin of such high ZT value is a liquid-like arrangement of Cu ions, which results in a very low lattice thermal conductivity [9]. The copper deficiency in the β-phase of $Cu_{2-x}Se$ ($x>0$) was also found to be a determinative factor for good electrical conductivity.

Research on synthesis and improvement of the chalcogenides for thermoelectric applications is currently one of the main subjects of interest for many researchers. Similarly in this work, we focused on a class of rare-earth copper chalcogenides $RECuCh_2$ (Ch= Se and Te). The results of this research are also available online in two published papers [41, 42].

3. Experimental Section

3.1. Synthesis methods

All samples were prepared by mixing stoichiometric ratios of the constituents in an argon filled glove-box, to exclude oxygen or moisture. The rare-earth elements and copper were filed in the glove-box and mixed with the powders of selenium or tellurium to facilitate their solid-state reaction. The mixtures were cold-pressed into 0.5 grams pellets. The pellets were placed in dried silica tubes and then evacuated and sealed under 10^{-5} Torr pressure. The samples were heated up to a certain temperature, kept for a few hours and annealed at lower temperatures. The prereacted samples were reground and repressed in the glove-box.

The selenide samples containing Er and Dy were heated up to 1050°C, kept for 6 hrs and annealed at 800°C for 100 hrs. For Gd, the annealing temperature was set at 700°C. For samples containing Sm and Pr, the preheating temperature was at 900°C and annealing at 600°C. The telluride samples containing RE = Er and Dy were heated to 1050°C, kept for 6 hrs and annealed at 800°C for 100 hrs. For RE = Gd, the annealing temperature was set at 700°C.

For $SmCuSe_2$ and $GdCuSe_2$, X-ray quality single crystals were directly obtained after the second or third heating. For the other samples, a chemical vapor transport (CVT) method was used to obtain suitable crystals. In this regard, about 200 mg of the annealed samples were placed with 50 mg of I_2 (solid) into 20 cm long silica tubes. The tubes were evacuated, flame sealed and put into a two-zone furnace for 240 hrs, with the sample being in the hot zone at 900°C and the growth zone having the temperature of 800°C.

However, no X-ray quality single crystals were obtained even after the third annealing for telluride containing samples. To obtain crystals, small fractions of the samples were annealed at 1000°C for 300 hrs. This treatment produced some shiny, flat, hexagonal crystals on the surfaces of the bulk samples.

3.2. Analysis methods

3.2.1. Powder X-ray diffraction

The wavelength range of the X rays (0.1-100Å) makes them suitable for studying materials on the atomic scale. For solid state materials in particular, the atomic structure of a compound at the short or large ranges can be investigated. Precise knowledge of elemental composition and atomic arrangement is required for understanding the relationship between the crystal structure and physical properties. This shall result in preparing new materials with an improved power factor. For instance, the idea of “PGEC” which was suggested by Slack et al [2] has led to a striking increase in ZT values for some structures, e.g. in skutterudites and clathrates. Nowadays, X-ray analysis is used to study a wide range of materials from crystalline solids to proteins. The major use of this method in this work was for characterization of the crystal structures of the synthesized ternary phases.

The *RE*CuSe$_2$ and *RE*CuTe$_2$ samples were analyzed by X-ray powder diffraction on a PANalytical X’pert Pro diffractometer with a CuK$_{\alpha 1}$ radiation and an X’celerator detector. Diffraction data were collected in the 2θ range of 20-70°. A full-profile Rietveld refinement (Rietica program [10]) was used to obtain the lattice constants and to evaluate sample purity. The atomic parameters from the single crystal refinements and literature were used for the Rietveld analysis. A representative refinement pattern for DyCuSe$_2$ and GdCuSe$_2$ is shown in Figure 6, which is similar for the other selenium containing samples with relevant monoclinic or trigonal structures.

Table 1. Space groups, number of formula units per cell (*z*), and lattice parameters for *RE*CuSe$_2$.

RE	**Sp. gr.**	***z***	**a/Å**	**b/Å**	**c/Å**	**β/ °**	**Volume/Å^3**	**Ref.**
Pr	$P2_1/c$	4	6.740(1)	7.481(1)	7.141(1)	97.36(5)	357.10(3)	34
	$P2_1/c$	4	6.7495(3)	7.4599(3)	7.1499(3)	97.367(3)	358.47(3)	Our work
Sm	$P2_1/c$	4	6.6655(6)	7.3825(7)	7.0724(6)	97.10(5)	345.34(7)	34
	$P2_1/c$	4	6.6783(4)	7.3895(4)	7.0856(4)	97.159(3)	346.94(4)	Our work
Gd	$P2_1/c$	4	6.6408(3)	7.3279(5)	7.0400(4)	96.97(3)	340.05(2)	34
	$P2_1/c$	4	6.6531(1)	7.3416(1)	7.0572(1)	97.040(1)	342.11(1)	Our work
Dy	$P\bar{3}m1$	1	4.070(1)	4.070(1)	6.459(2)	90	92.65(6)	11
	$P\bar{3}m1$	1	4.07513(7)	4.07513(7)	6.4447(1)	90	92.830(3)	Our work
Er	$P\bar{3}$	1	4.0407(1)	4.0407(1)	6.4420(3)	90	91.09(1)	33
	$P\bar{3}m1$	1	4.04691(5)	4.04691(5)	6.44643(9)	90	91.432(2)	Our work

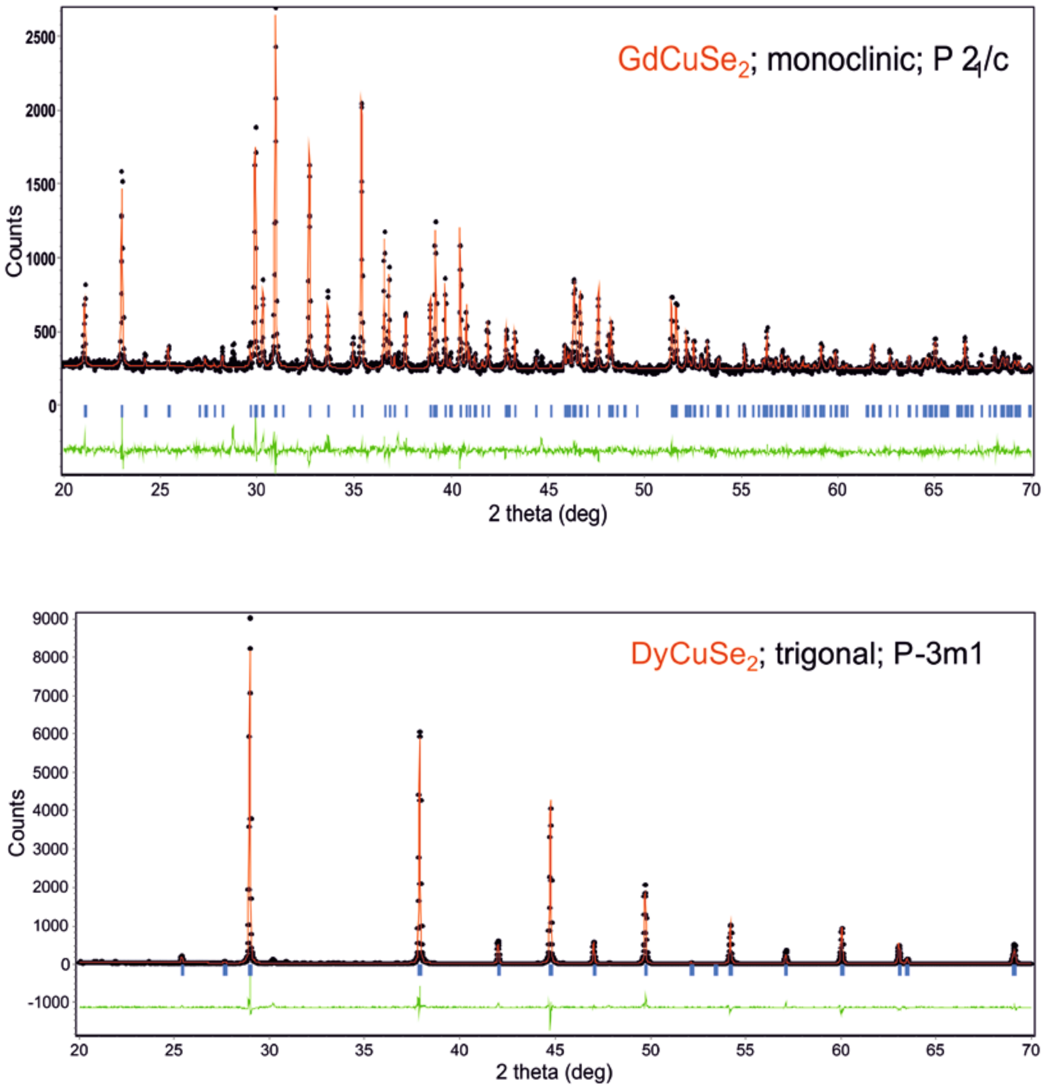

Figure 6. Rietveld refinement of the X-ray powder data for $DyCuSe_2$ and $GdCuSe_2$.

As shown in Figure 7 for $DyCuTe_2$, some peaks are split, which is indicative of the symmetry lower than $P\bar{3}$m1 reported in the literature (12). Identical splitting was observed for $GdCuTe_2$ and $ErCuTe_2$. Since the general features of the $DyCuTe_2$ powder pattern are similar to those expected for the $P\bar{3}$m1 structure, we speculated that the space group for $DyCuTe_2$ is subgroup of $P\bar{3}$m1. Using the single crystal techniques, the structure was successfully solved in the $C2/m$ space group. The

Rietveld refinement of the $DyCuTe_2$ sample with the $C2/m$ model is shown in Figure 7. The peak splitting and peak intensity are well described with this model. There are small unknown impurities in the sample. The powder patterns of $GdCuTe_2$ and $ErCuTe_2$ were also successfully refined with the $C2/m$ model.

Table 2. Space groups, number of formula units per cell (z), and lattice parameters for *RE*$CuTe_2$.

RE	**Sp. gr.**	**z**	**a/Å**	**b/Å**	**c/Å**	**β/ °**	**Volume/Å^3**	**Ref.**
Gd	$P\bar{3}c1$	1	4.190	4.190	7.223	90	340.05(2)	39
	$C2/m$	2	7.4781(5)	4.3382(3)	6.9279(4)	90.182(5)	224.75(3)	Our work
Dy	$P\bar{3}m1$	8	8.619(1)	8.619(1)	13.857(1)	90	841.5(3)	29
	$P\bar{3}$	1	4.2974(3)	4.2974(3)	6.9074(7)	90	110.47(3)	40
	$C2/m$	2	7.4147(6)	4.3068(3)	6.9036(5)	90.302(5)	220.45(3)	Our work
Er	$P\bar{3}c1$	1	4.200	4.200	7.150	90	109.23(1)	39
	$C2/m$	2	7.382(7)	4.2864(4)	6.8947(6)	90.306(7)	218.16(3)	Our work

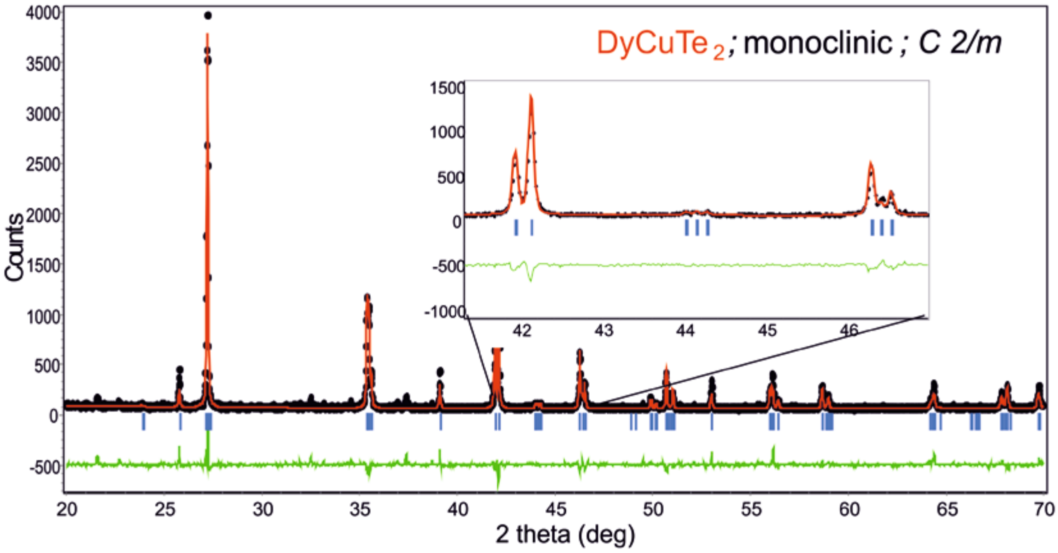

Figure 7. Rietveld refinement of $DyCuTe_2$ with $C2/m$ space group; peak split shown in inset. Because of the principal similarities between this pattern and the pattern

found for $DyCuTe_2$ with *P*-3m1 structure, we assume the *C*2/m is a subgroup of *P*-3m1.

3.2.2. Single crystal X-ray diffraction

Crystals suitable for single crystal X-ray diffraction experiments are typically 0.1-0.5 mm in size. A crystal is mounted on a glass capillary with epoxy glue and collected on a STOE IPDSII diffractometer with an image plate detector and a Mo*K*α radiation in the whole reciprocal sphere at room temperature. After collecting all the diffracted peaks, the reciprocal lattice and then the unit cell in real space are extracted. A numerical absorption correction is based on the crystal shape defined using optical face indexing. It is optimized afterwards against equivalent reflections with the STOE X-shape software [11]. Structural refinements are performed using the SHELXTL program [12].

In a single crystal refinement, similar to the powder diffraction method, the least square method is used in order to minimize the difference between the experimental and calculated intensities. In this respect, a number of parameters are refined including: the type of elements, the atomic coordinates and occupancy, the anisotropic thermal parameters and the extinction coefficient.

In the monoclinic structures of $SmCuSe_2$ and $GdCuSe_2$, all sites were fully occupies. In the trigonal structure of $DyCuSe_2$, the Cu atoms randomly fill 50% of the 2*d* (1/3, 2/3, z) site, while the Dy and Se atoms occupy fully the 1*a* (0, 0, 0) and 2*d* (1/3, 2/3, z) sites, respectively. The trigonal space groups of lower symmetry were tested for $DyCuSe_2$, but the random distribution of the Cu atoms remained. The orthorhombic or monoclinic distortions were not considered, as the powder pattern of $DyCuSe_2$ did not support any lattice distortions. It has to be mentioned that the atomic structure of $DyCuSe_2$ is identical to those reported for $HoCuSe_2$ and $ErCuSe_2$ from the single crystal data [33], but the space group is $P\bar{3}m1$ instead of reported $P\bar{3}$ (the mirror plane was missed by the previous authors).

For the tellurium-containing phases, no crystals suitable for X ray diffraction could be picked up from the $RECuTe_2$ (RE= Gd, Dy) samples, and only data for $DyCuTe_2$ were successfully collected. Analysis of the reciprocal space did not indicate presence of a superstructure. However some of the diffraction spots were broad or slightly split, suggesting a symmetry lower than $P\bar{3}$m1 and presence of at least two twin components. Because of the relatively poor angular resolution of the image plate and spots' overlap, the indexing of the diffraction spot would yield lattice constants representative of a trigonal unit cell. Assuming that the symmetry lowering follows the group-subgroup relationship, we tested the monoclinic symmetry ($C2/m$ space group) first. The structural solution proceeded well, but significant residual electron density remained. Introducing a twin law significantly improved the refinement and yielded a much smoother residual electron density.

In the monoclinic $DyCuTe_2$, the Cu atoms randomly fill 50% of the 4*i* (0.6660, 0, 0.6377) site, while the Dy and Te atoms fully occupy the 2*a* (0, 0, 0) and 4*i* (0.3333, 0, 0.7407) sites, respectively. The monoclinic space groups of lower symmetry (*C*2 and *Cm*) were tested for $DyCuTe_2$, but the random distribution of the Cu atoms remained. The orthorhombic distortions were not considered, as the powder pattern of $DyCuTe_2$ did not support this type of distortion. The refinement results are summarized in Tables 3-6.

Table 3. Crystallographic and refinement parameters for the *RE*$CuSe_2$ and $DyCuTe_2$ single crystals

	$SmCuSe_2$	$GdCuSe_2$	$DyCuSe_2$	$DyCuTe_2$
Space group	$P2_1/c$	$P2_1/c$	$P\bar{3}m1$	$C2/m$
Unit cell dimensions	a = 6.668(1) Å b = 7.380(1) Å c = 7.069(1) Å β = 97.12(3)°	a = 6.641(1) Å b = 7.328(1) Å c = 7.040(1) Å β = 96.97(3)°	a = 4.0669(6) Å c = 6.445(1) Å	a = 7.448(1) Å b = 4.3019(9) Å c = 6.898(1) Å β = 90.05(3)°
Volume, $Å^3$	345.15(2)	340.05(2)	92.32(3)	221.04(8)
Wavelength, Å	0.71073	0.71073	0.71073	0.71073
Z	4	4	1	2
Density (calculated), g/cm^3	7.155	7.398	6.906	7.231
Absorption coefficient, mm^{-1}	43.809	46.700	45.279	34.293
Measured reflections	3757	3999	958	2301
Goodness-of-fit on F^2	1.070	1.124	1.180	1.087
R indices [$I > 2\sigma(I)$]	R_1 = 0.0446, wR_2 = 0.1101	R_1 = 0.0567, wR_2 = 0.1483	R_1 = 0.0127, wR_2 = 0.0208	R_1 = 0.0430, wR_2 = 0.1138
R indices (all data)	R_1 = 0.0590, wR_2 = 0.1259	R_1 = 0.0592, wR_2 = 0.1508	R_1 = 0.0183, wR_2 = 0.0212	R_1 = 0.0459, wR_2 = 0.1156

Table 4. Atomic coordinates and equivalent isotropic displacement parameters, U_{eq} for the *RE*CuSe$_2$ and DyCuTe$_2$ single crystals.

Atoms	Site	Occ.	*x*	*y*	*z*	U_{eq}, Å^2
			SmCuSe$_2$			
Sm	4e	1	0.3060(1)	0.4531(1)	0.1987(1)	0.009(1)
Cu	4e	1	0.0759(2)	0.8392(2)	0.0505(2)	0.018(1)
Se(1)	4e	1	0.5765(1)	0.2257(1)	0.0011(1)	0.009(1)
Se(2)	4e	1	0.0978(1)	0.6106(1)	0.2184(1)	0.010(1)
			GdCuSe$_2$			
Gd	4e	1	0.3052(1)	0.9541(1)	0.1984(1)	0.010(1)
Cu	4e	1	0.0788(2)	0.3406(2)	0.0501(2)	0.019(1)
Se(1)	4e	1	0.5733(1)	0.7257(1)	0.0008(1)	0.009(1)
Se(2)	4e	1	0.0976(1)	0.1114(1)	0.2174(1)	0.010(1)
			DyCuSe$_2$			
Dy	1a	1	0	0	0	0.0010(1)
Cu	2d	0.570(7)	1/3	2/3	0.6244(3)	0.0022(1)
Se	2d	1	1/3	2/3	0.2501(1)	0.0010(1)
			DyCuTe$_2$			
Dy	2a	1	0	0	0	0.015(1)
Cu	4i	0.5	0.6660(6)	0	0.6377(7)	0.022(1)
Te	4i	1	0.3333(1)	0	0.7407(1)	0.012(1)

Table 5. Interatomic distances (Å) for SmCuSe$_2$ and GdCuSe$_2$. Number of bonds per unit cell is given in the parenthesis.

SmCuSe$_2$			
Sm-Se(1) (×2)	2.908(2)	Sm-Se(1) (×2)	2.924(3)
Sm-Cu (×2)	3.385(8)	Sm-Se(1) (×2)	2.969(2)
Sm-Se(2) (×2)	2.977(2)	Cu-Se(1) (×2)	2.434(7)
Sm-Se(2) (×2)	3.134(3)	Cu-Se(2) (×2)	2.513(1)
Sm-Cu (×2)	3.440(7)	Cu-Se(2) (×2)	2.578(1)
Sm-Se(2)	2.952(1)	Cu-Se(2)	2.436(8)
Sm-Se(1)	2.949(2)	Sm-Cu	3.342(6)
Cu-Cu	2.644(3)		

GdCuSe_2			
Gd-Se(1) (×2)	2.892(1)	Cu-Se(2) (×2)	2.512(7)
Gd-Se(1) (×2)	2.911(2)	Cu-Se(2) (×2)	2.566(1)
Gd-Se(1) (×2)	2.954 (1)	Gd-Se(2) (×2)	2.959(1)
Gd-Se(2) (×2)	3.118(1)	Gd-Cu	3.316(1)
Gd-Cu (×2)	3.380(2)	Gd-Cu (×2)	3.399(6)
Cu-Se(1) (×2)	2.427(6)	Cu-Se(2)	2.432(6)
Gd-Se(1)	2.923 (1)	Gd-Se(2)	2.931(1)
Cu-Cu	2.621(3)		

Table 6. Interatomic distances (Å) for $DyCuSe_2$ and $DyCuTe_2$. Numbers of bonds per unit cell are in the parenthesis.

DyCuSe_2			
Dy-Se (×8)	2.8482(5)	Dy-Cu (×9)	3.372 (1)
Cu-Se (×6)	2.4833(7)		
Cu-Cu (×3)	2.843(2)		
Cu-Se	2.412(2)		

DyCuTe_2			
Dy–Te (×4)	3.0600(9)	Cu–Te (×1)	2.578(5)
Dy–Te (×2)	3.062(1)	Cu–Te (×2)	2.585(3)
Dy–Cu (×4)	3.522(4)	Cu–Te (×1)	2.610(5)
Dy–Cu (×2)	3.525(5)		

3.2.3. Energy Dispersive X-ray Spectroscopy (EDS)

In order to confirm the composition of the samples, an EDS analysis was carried out on the single crystals using a JEOL 7000F scanning electron microscope. Copper metal was used as standard to calibrate the signals. The atomic percentages of elements were obtained from 3-5 points on the crystals surfaces. No contamination from the silica tubes was observed.

Table 7. The EDS compositions for the *RE*CuSe$_2$ and DuCuTe$_2$ phases.

RE	Atomic % of *RE*/Cu/Se(Te)[1]	Normalized to 4 atoms
Sm	25(3) | 25(2) | 50(5)	$Sm_{1.0(1)}Cu_{1.00(8)}Se_{2.0(2)}$
Gd	25(1) | 22(1) | 53(1)	$Gd_{1.00(4)}Cu_{0.88(4)}Se_{2.12(4)}$
Dy	25(3) | 28(3) | 47(6)	$Dy_{1.0(1)}Cu_{1.1(1)}Se_{1.9(2)}$
Dy[1]	24(2) | 25(1) | 51(1)	$Dy_{1.0(1)}Cu_{1.0(1)}Te_{2.1(2)}$

3.2.4. Differential Thermal and Gravimetrical Analyses (DTA and TGA)

The stability of the samples was tested using differential thermal and gravimetrical analysis (DTA and TGA) on “NETZSCH STA 409 PC/PG” over a temperature range from 25 to 600 or 800°C in argon atmosphere. Any thermal event like melting, decomposition or crystal structure change could be traced by these tests. Based on the TGA results (Figure 8), GdCuSe$_2$ is stable up to around 500°C and decomposes at higher temperatures, while ErCuSe$_2$ start to lose mass above 325°C. The nature of the DTA plateau between 250 and 300^{o}C for GdCuSe$_2$ is not well understood, but may be related to sublimation of free Se from the bulk sample.

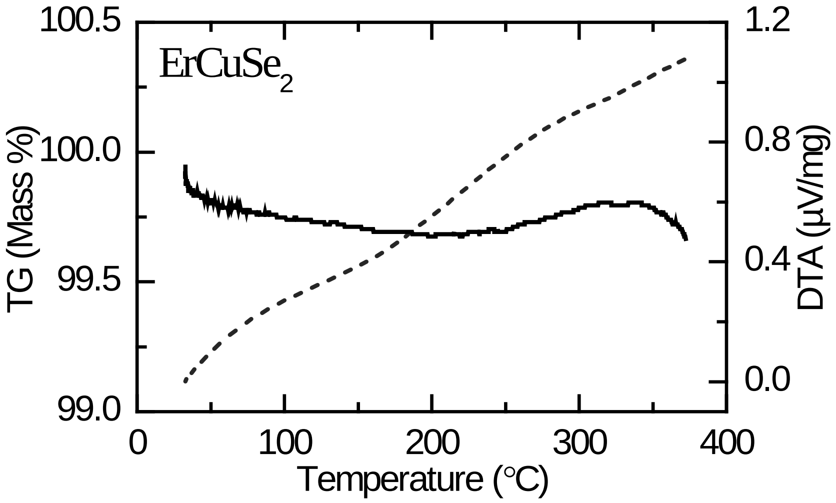

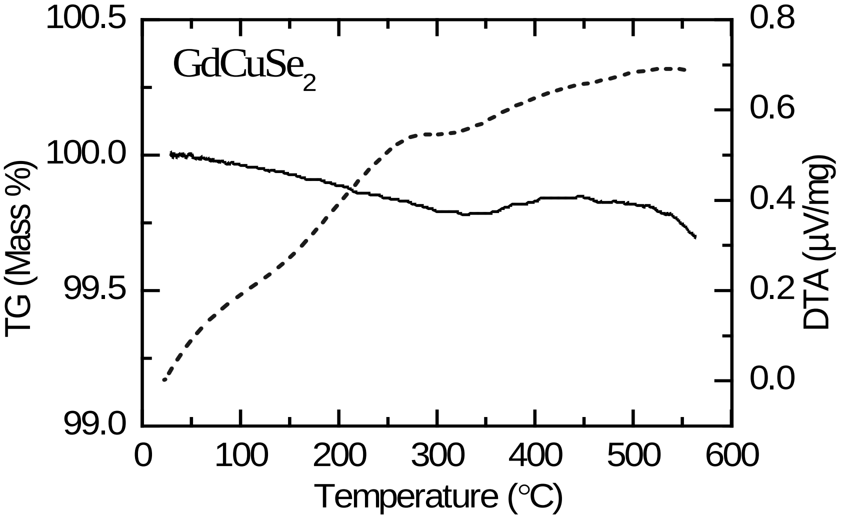

Figure 8. The DTA (dashed) and TGA (solid) curves for $GdCuSe_2$ and $ErCuSe_2$.

Based on the TGA results in the Te-containing series (Figure 9), $GdCuTe_2$ is stable up to 800°C, $DyCuTe_2$ up to 700°C and $ErCuTe_2$ up to around 400°C. $DyCuTe_2$ and $ErCuTe_2$ start to decompose at higher temperatures. Since there is no substantial difference between the three Te-samples, we may attribute the increase in mass in the TGA curve for $ErCuTe_2$ to the instrumental errors.

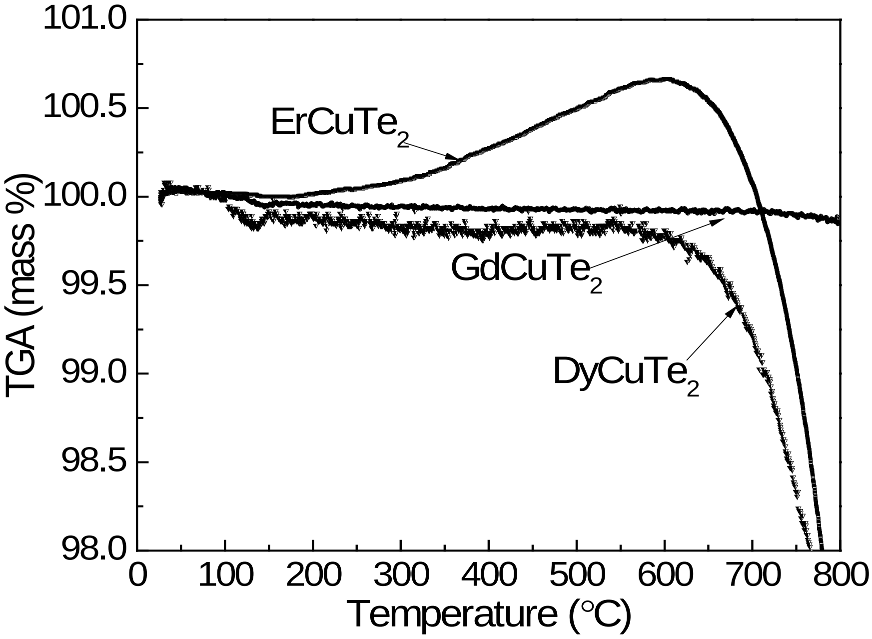

Figure 9. The TGA curves for $DyCuTe_2$, $GdCuTe_2$ and $ErCuTe_2$.

3.2.5. Physical properties measurement

The cold-pressed consolidated pellets were cut into rectangular bars with the dimensions of ~7 × 2× 2 mm^3. Seebeck coefficient (S) and electrical resistivity (σ) were measured in the temperature range from 30 to 500°C on a ZEM series system (ZEM-3; ULVAC, USA).

3.2.6. Electronic band structure calculations

The electronic structures of all the samples were calculated using the tight-binding, linear-muffin tin orbital method with the atomic atmosphere approximation (TB-

LMTO-ASA [14]). The lattice constants and atomic parameters from the single crystal refinements of *RE*CuSe$_2$ (*RE* = Gd and Dy) were used for the calculations. The *RE f*-electrons were considered as core electrons that are localized and do not participate in bonding. For DyCuSe$_2$, the following structural model of a lower symmetry, *P*3m1, was used to make the site occupancy equal to unity for Cu atoms. In this model, the Dy atoms occupy the 1*a* (0, 0, 0) site, the Cu atoms the 1*b* (1/3, 2/3, 0.6244) site, the Se1 atoms the 1*b* (1/3, 2/3, 0.25014) site and the Se2 atoms the 1*c* (2/3, 1/3, 0.74986) site. To have full occupancy for the Cu atoms in DyCuTe$_2$, the *C*m space group was used for the LMTO calculations. In this structural model, the Dy, Cu, Te1 and Te2 atoms occupy 2a (0, 0, 0), 2a (0.6660, 0, 0.6377), 2a (0.3333, 0, 0.7407) and 2a (0.6666, 0, 0.2593) sites, respectively.

4. Results and discussion

4.1. Crystal structure

4.1.1. *RE*CuSe$_2$

The *RE*CuSe$_2$ compounds crystallize with either the monoclinic LaCuS$_2$ structure (*P*2$_1$/*c* [15, 16]) for the light *RE* elements, *RE* = Gd, Pr, Sm [34], or Cu-deficient trigonal ErCu$_2$S$_2$ structure ($P\overline{3}$m1 [36, 37]) for heavier *RE* = Dy, Er [33, 11]. I will discuss the trigonal structure first and focus on the DyCuSe$_2$ representative (Figure 10). In this structure, the Se atoms form a hexagonal close packing, and the Cu atoms randomly occupy 50% of the tetrahedral voids in one layer, while the Dy atoms fill all the octahedral voids in the adjacent layers. The Dy-Se and Cu-Se distances (Table 6) are close to the sum of atomic radii (r_{Dy} = 1.78 Å, r_{Se} = 1.16 Å, r_{Cu} = 1.28 Å) [17].

Since Cu-filled Se tetrahedra share edges, there are Cu-Cu distances of 2.84 Å, but they are too long for significant Cu-Cu interactions.

In the monoclinic $GdCuSe_2$ structure, the Se atoms form two highly puckered layers (Figure 4, right). One made of the Se1 atoms at x =0.43 and 0.57 resembles a distorted square layer, while the other composed of the Se2 atoms at x = -0.1 and 0.1 is a distorted hexagonal one. The layers stack in the *ABAB* sequence along the *a* direction and make the distorted tetrahedral and seven-vertex voids. The smaller tetrahedral voids are filled with Cu, and the larger seven-vertex ones are occupied by Gd. Two Cu-filled Se tetrahedra in the trans position share an edge to form Cu_2Se_7 units, which in turn share corners with other Cu_2Se_7 units to make a two-dimensional, 2D, $CuSe_2$ layer within the *bc* plane. The 2D $CuSe_2$ layers joined through the Gd atoms. The Cu-Cu distances within the Cu_2Se_7 units are relatively short, 2.62 Å, but longer than the Cu-Cu ones of 2.52 Å in Cu_2Se [18]. These Cu-Cu interactions will be explored later via electronic structure analysis. The Gd-Se distances range from 2.89Å to 3.12Å (Table 5), are close to the sum of atomic radii ($r_{\mathrm{Gd}}+ r_{\mathrm{Se}}$= 1.80Å+ 1.16Å = 2.96Å) [17] and analogous to the Gd-Se bonds observed in the binary systems, i.e. Gd_2Se_3 [19] and Gd_3Se_4 [20]. The Cu-Se distances vary between 2.43Å to 2.57Å in $GdCuSe_2$ and are close to the sum of atomic radii ($r_{\mathrm{Cu}}+ r_{\mathrm{Se}}$= 1.28Å+ 1.16Å =2.44 Å) [17].

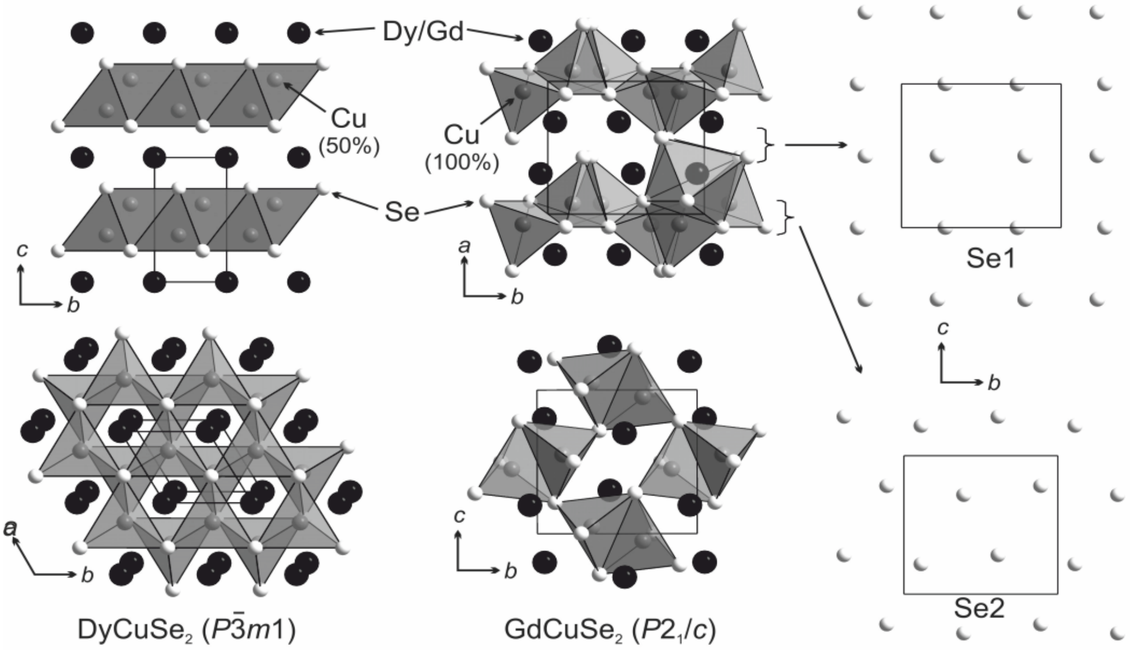

Figure 10. (left) $DyCuSe_2$ structure, emphasizing the Se tetrahedra filled with Cu. (center) $GdCuSe_2$ structure, emphasizing the Se tetrahedra filled with Cu. The Gd-filled Se polyhedron is shown in the top figure. (right) The Se1 and Se2 layers of the $GdCuSe_2$ structure.

The stability of the monoclinic and trigonal *RE*$CuSe_2$ structures appears to be directly related to the size of the rare-earth atoms. The monoclinic structure, which offers larger coordination spheres for the rare-earth atoms, is found for earlier rare earths, while the trigonal structure with tighter *RE* environments is preferred for later rare earths.

4.1.2. ***RE*CuTe₂**

The *RE*$CuTe_2$ compounds crystallize with a Cu-deficient monoclinic structure (*C*2/m, *z* = 2, Figure 5) for *RE* = Gd, Dy and Er. This monoclinic structure is a distorted variant of the $P\bar{3}m1$ structure observed in $DyCuSe_2$ and $ErCuSe_2$. In the *C*2/m structure, the Te atoms form a hexagonal close packing (*ABAB*... sequence along the *c* direction), and the Cu atoms randomly occupy 50% of the tetrahedral voids in one layer, while the Dy atoms fill all the octahedral voids in the adjacent layers. The Dy-Te and Cu-Te distances (Table 4) are slightly smaller than the sum of atomic radii (r_{Dy} = 1.78 Å, r_{Te} = 1.40 Å, r_{Cu} = 1.28 Å) [17], which is due to the facts that the atomic radii quoted for Dy and Cu are for the coordination number of 12 observed in pure elements. The Dy-Te distance are similar to those found in other ternary compounds, e.g. 3.032(3) Å in $Dy_7Cu_3Te_{12}$ [21], 3.057 Å in $DyCu_3Te_3$ [22] and 3.050(1) Å in $DyCu_{0.32}Te_2$ [23], or binary compounds, e.g. 3.048-3.066 Å in Dy_2Te_3 [24], 3.063-3.141(5) Å in Dy_2Te [25] and 3.06 Å in DyTe [26]. The Cu-Te distances are similar to 2.661 Å in $DyCu_3Te_3$ [22], 2.503, 2.611 Å in Cu_2Te [27] and 2.484(3), 2.652(5) Å in $Cu_{1.81}Te$ [28].

The monoclinic distortion in *RE*CuTe$_2$ is relatively small, and based on the inter-atomic distances in $DyCuTe_2$, it can be attributed to the Cu displacements, which in turn are driven by the larger size of the Te atoms as compared to the Se atoms ($DyCuSe_2$ adopts the $P\bar{3}m1$ structure). While the Dy atoms have almost identical distances to 6 Te atoms, the Cu atoms have 1 out of 4 Te atoms at a longer distance. Being situated inside the Te tetrahedra, the Cu atoms are shifted along the *c* axis from the apical Te atoms towards the Te faces parallel to the ab plane (Table 6). Likely, such the displacement leads to optimized bonding between the Cu and Te atoms.

The *C*2/m structure for *RE*CuTe$_2$ is similar to the $P\bar{3}m1$ one reported for $DyCuTe_2$ by Gulay at el. from the single crystal data [29]. The $P\bar{3}m1$ structure of $DyCuTe_2$ is a superstructure of the $P\bar{3}m1$ one observed for $DyCuSe_2$ and has all the unit cell parameters doubled. Out of the 3 Cu sites in the $P\bar{3}m1$ $DyCuTe_2$ structure, one site is fully occupied and two are partially occupied. This model of $DyCuTe_2$ has a very poor agreement with our experimental powder pattern for $DyCuTe_2$ and does not describe peak splitting. We cannot explain such structural discrepancy, expect for suggesting that the experimental conditions were different or the solution for the $P\bar{3}m1$ $DyCuTe_2$ structure needs to be revisited.

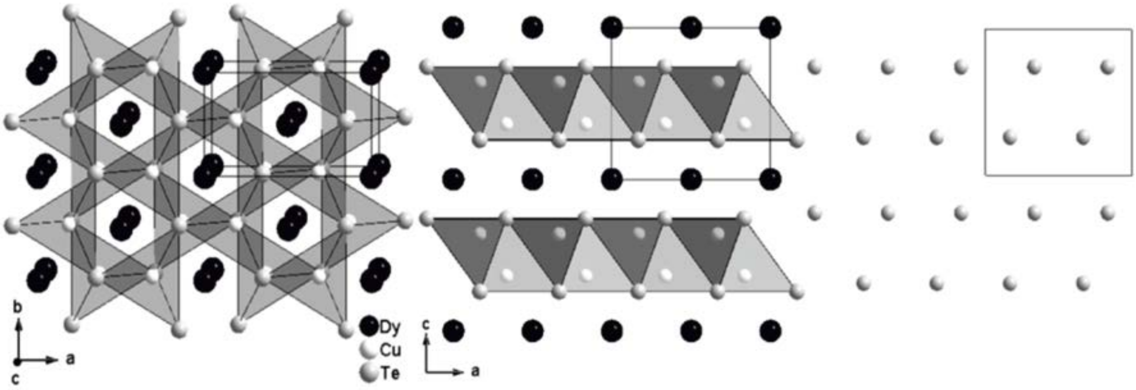

Figure 11. $DyCuTe_2$, Monoclinic ($C2$/m, z = 2), (right) Te atoms are packed in a hexagonal fashion. (Left) The Cu atoms occupy 50% of the tetrahedra generated by Te atoms.

4.2. Electronic structure

4.2.1. *RE*$CuSe_2$

Considering that there are no short Dy-Dy, Dy-Cu, Cu-Cu or Se-Se interactions in $DyCuSe_2$, the electronic formula can be written as $(Dy^{3+})(Cu^{+})(Se^{2-})_2$ and is charge balanced. The valence band should be dominated by Se *p* states around the Fermi level and by the Cu *d* states at lower energies. The conduction band, composed primarily of the Dy *d* states, is likely to be separated from the valence band via a band gap.

Prediction of the electronic formula for $GdCuSe_2$ is not as straightforward due to the presence of the short Cu-Cu distances of 2.62 Å. If we assume that these Cu-Cu distances stem from the matrix effect, i.e. dictated by the position of the Se and Gd atoms, the electron formula will be similar to that of $(Dy^{3+})(Cu^{+})(Se^{2-})_2$ and charge balanced: $(Gd^{3+})(Cu^{+})(Se^{2-})_2$. Likewise, if we assume the presence of the Cu-Cu dimers, we will arrive at the same charge balance formula. The Cu *d* orbitals are completely full (d^{10} configuration), and the pure d^{10}-d^{10} interactions are repulsive. However, hybridization of the *d* orbitals with empty, higher-energy *s* and *p* orbitals ($d_z{}^2$, *s* and p_z ones if the *z* axis is chosen along the Cu-Cu dimer) leads to the larger stabilization of both bonding and antibonding σ-type bonds derived from the *d* orbitals within the Cu-Cu dimers [30]. Such stabilization of the d^{10}-d^{10} interactions does not change the electron count for Cu, and the $(Dy^{3+})(Cu^{+})(Se^{2-})_2$ formula is still applicable.

These qualitative arguments for $DyCuSe_2$ and $GdCuSe_2$ are supported by the electronic structure calculations (Figure 12). In each case, the conduction band is dominated by the *RE* *d* states, while valence band is dominated by the Se *p* states at the low- and high-energy regions and by the Cu *d* states in the middle. Due to the lower symmetry of $GdCuSe_2$ (more bonds with different lengths), the DOS features, e.g. DOS maxima, are broader in the valence and conductions bands. There are band gaps in the both structures, with a larger band gap being observed in $GdCuSe_2$ (0.87 vs. 0.64 eV) due to the more electropositive nature of Gd as compared to Dy. The Cu-Cu interactions for $GdCuSe_2$ were analyzed in terms of the crystal orbital Hamilton population, COHP (Figure 13). Below the Fermi level, the Cu-Cu interactions originate primarily from the *d* orbitals, and they are mostly bonding in nature due to the hybridization as discussed above. We have also calculated COHP curves for the Cu-Se and Gd-Se interactions (Figure 13), and as one would expect, the states below the Fermi level are bonding and those above are antibonding.

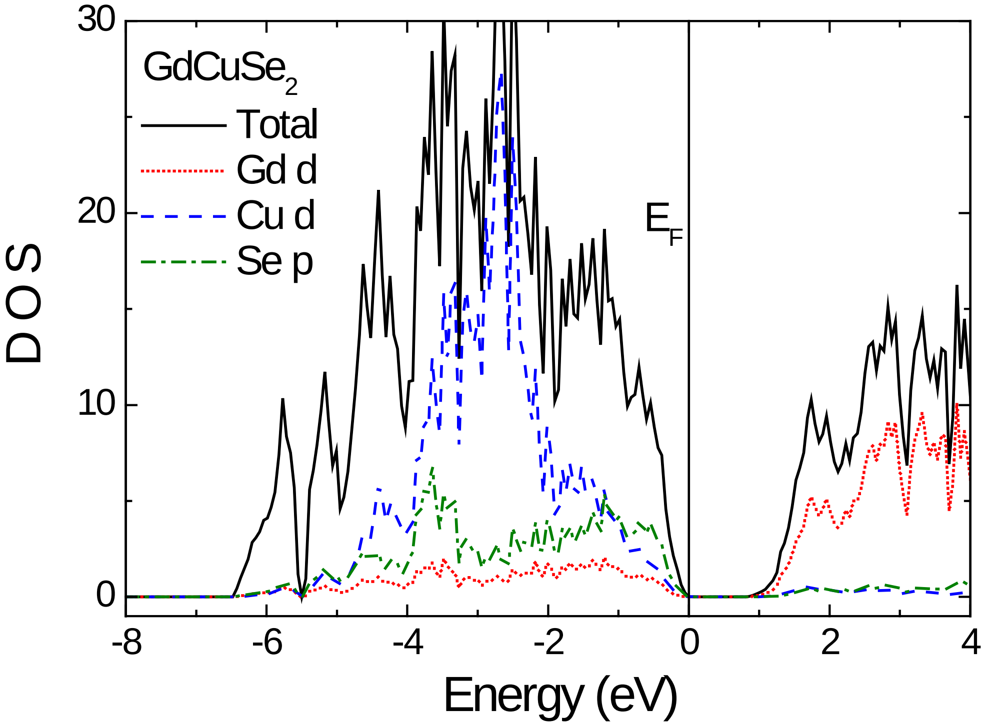

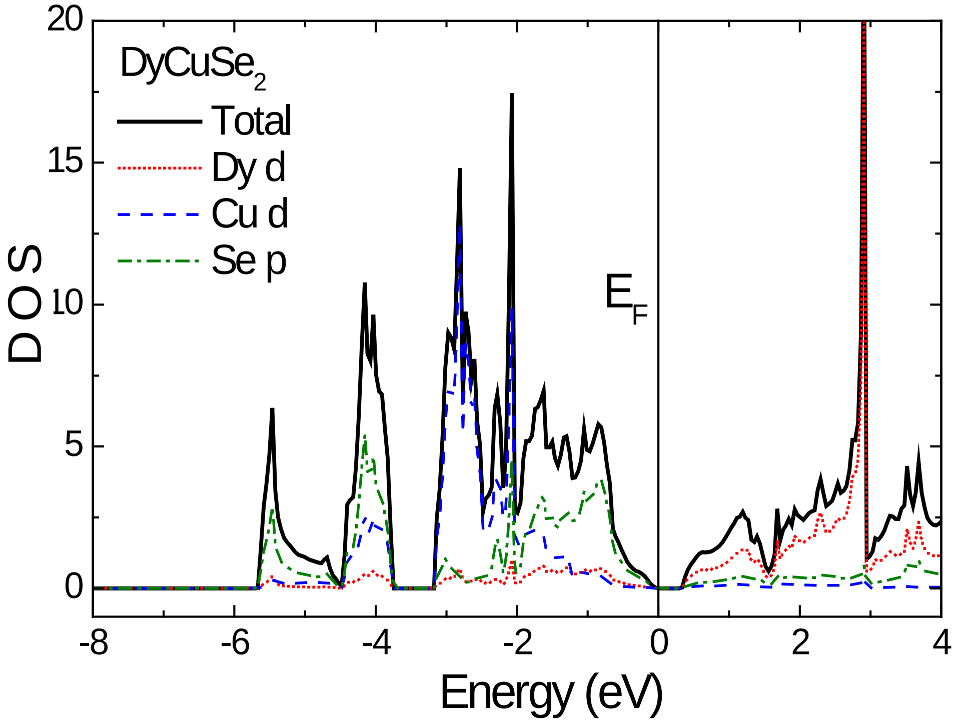

Figure 12. Total and partial densities of states (DOS) for $GdCuSe_2$ and $DyCuSe_2$.

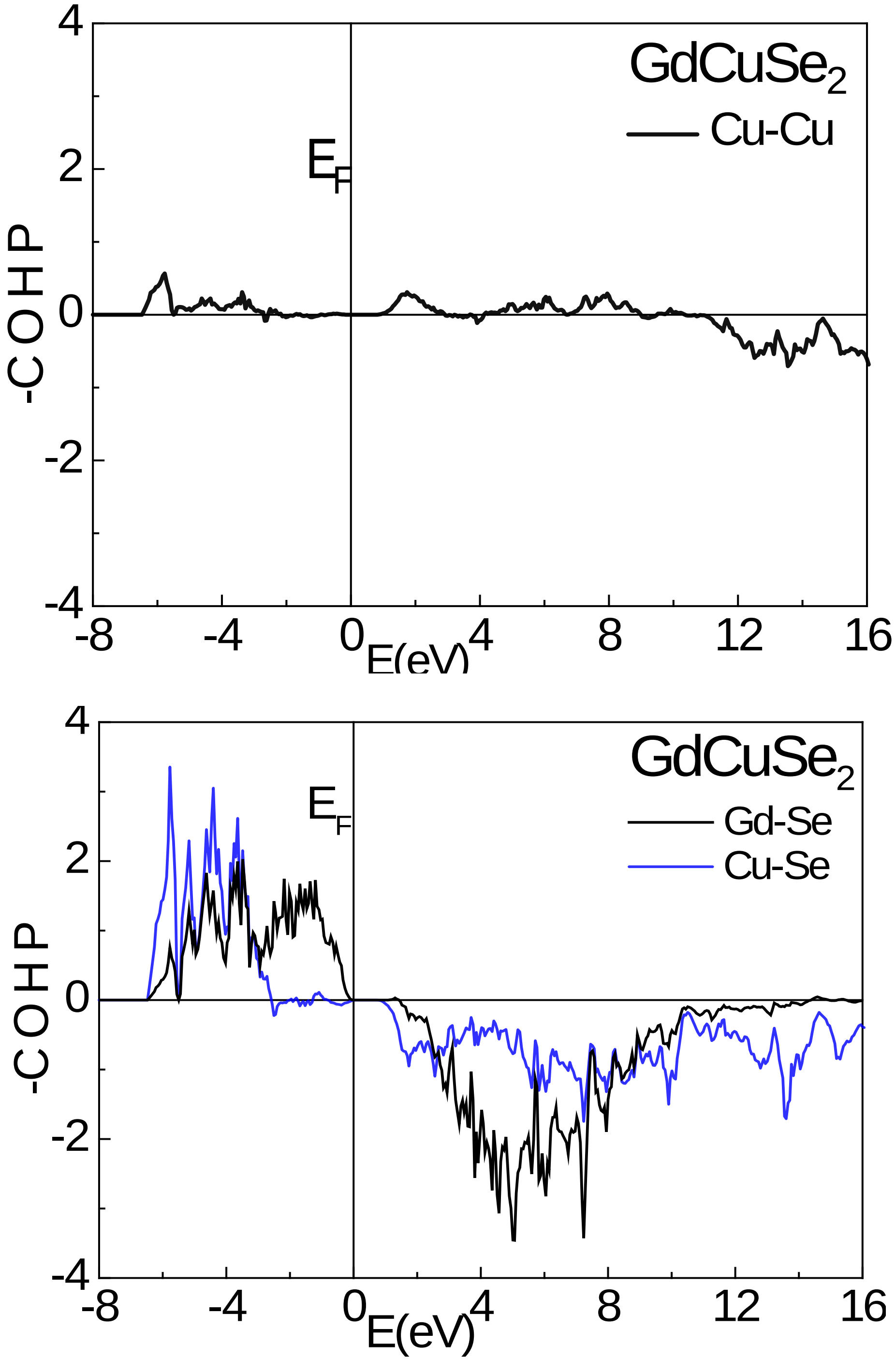

Figure 13. Bonding and antibonding between Cu-Cu and Cu-Se in GdCuSe$_2$ by COHP calculations.

4.2.2. ***RE*CuTe$_2$**

Since there are no close cation-cation or Te-Te interaction in DyCuTe$_2$, the electronic formula can be written as $(Dy^{3+})(Cu^{+})(Te^{2-})_2$ which is charge balanced. The valence band should be dominated by Te *p* states around the Fermi level and by the Cu *d* states at lower energies. The conduction band, composed primarily of the Dy *d* states, is likely to be separated from the valence band via a band gap.

The calculated electronic structures for DyCuTe$_2$ and DyCuSe$_2$ for comparison are given in Figure 14. In each case, the conduction band is dominated by the Dy *d* states, while valence band is dominated by the Se *p* or Te *p* states at the low and high-energy regions and by the Cu *d* states in the middle. There is a band gap in the DyCuSe$_2$ structure (0.64 eV) while a pseudo-gap is observed in the DyCuTe$_2$ structure. The absence of a band gap for DyCuTe$_2$ is due to the smaller electronegativity of Te as compared to Se. Based on the LMTO calculations, we may expect a metal-type resistivity for DyCuTe$_2$ (and other tellurides) while a semiconducting behavior for DyCuSe$_2$ (and other selenides). As shown below, the experimental resistivities support these arguments. A similar decrease in the band gap upon partial Te substitution was also observed in the *RE*CuS$_2$ phases (*RE*= Sm, La) [31]. While a band gap still remained in *RE*CuSTe, it was significantly smaller than that in *RE*CuS$_2$ (e.g. 1.54 and 0.62 eV for LaCuS$_2$ and LaCuSTe, respectively).

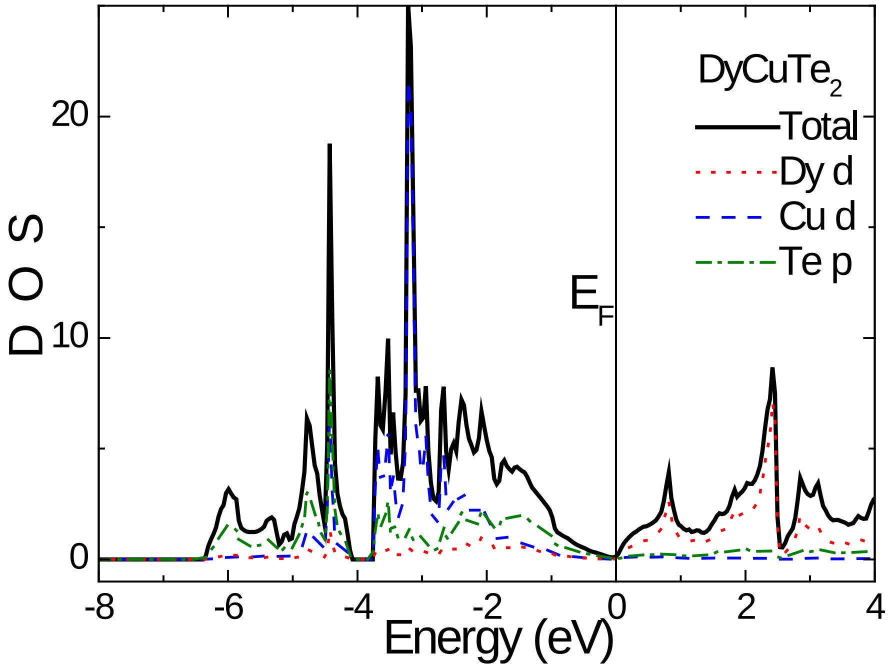

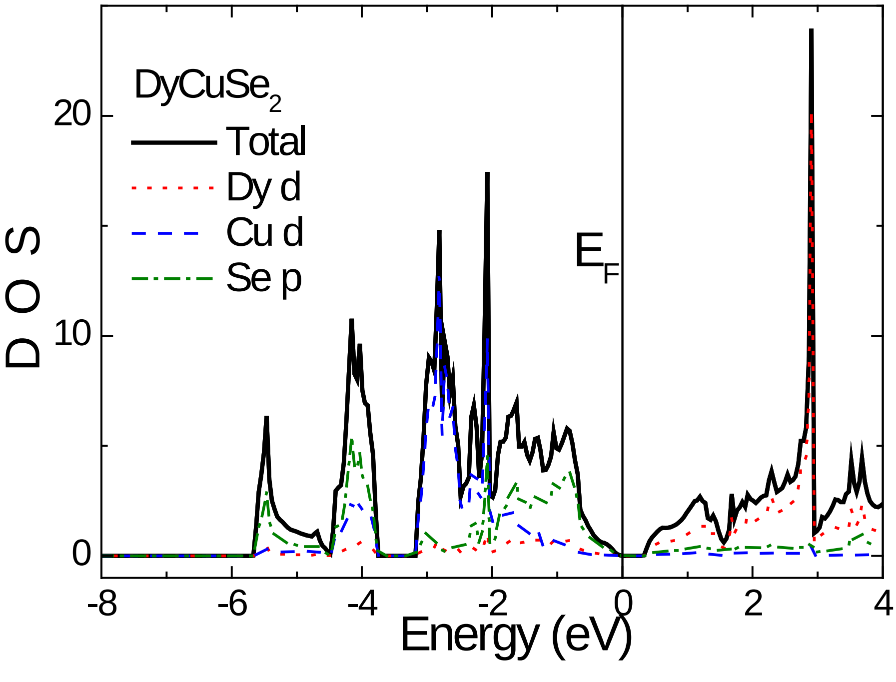

Figure 14. Total and partial densities of states (DOS) for $DyCuTe_2$ and $DyCuSe_2$.

4.3. Physical properties

The electrical resistivity of the $PrCuSe_2$, $GdCuSe_2$ and $DyCuSe_2$ samples decreases from room temperature till 500^oC and follows the Arrhenius law (Figure 15). The electrical resistivity of $SmCuSe_2$ remains unchanged, but decreases at higher temperatures. The Seebeck coefficients for $PrCuSe_2$, $SmCuSe_2$, $GdCuSe_2$ and $DyCuSe_2$ increase with temperature and reach the values of 408, 282, 150 and 170 μV/K at 500^oC, respectively. The electrical resistivity and Seebeck coefficient of $ErCuSe_2$ display similar behavior but only till 300^oC, at higher temperatures there are abrupt changes due to the sample decomposition. For all samples, the Seebeck coefficient is positive, indicating that dominant carriers are holes. The activation energies were calculated using the Arrhenius equation assuming that only holes contribute to the charge transport. Their values together with the electrical resistivity values at room temperature are given in Table 8. The electrical resistivities at room temperature are ~ 0.5-500 Ω cm, which are 2 to 5 orders of magnitude greater than the values for the high performance thermoelectric materials [32].

One interesting point is drastically different values of resistivity and Seebeck coefficient for $ErCuSe_2$ as compared to other selenides, which suggest that $ErCuSe_2$ is more insulating. Such discrepancy, especially between $ErCuSe_2$ and $DyCuSe_2$, is not understood since both phases adopt the same trigonal structure. Another point worth mentioning is that activation energies derived from the resistivity measurements are much smaller than band gaps calculated. While the LMTO method can overestimate band gaps, the discrepancy is too large and likely stems from the fact that activation energies measured do not represent the actual band gaps.

The electrical resistivity of $DyCuTe_2$ and $ErCuTe_2$ increases gradually with temperature, similar to metals (Figure 15). The electrical resistivities for $DyCuTe_2$ and $ErCuTe_2$ at room temperature are 0.022 and 0.082 Ωcm, respectively, which suggests that they are poor metals. The Seebeck coefficient of $ErCuTe_2$ increases with temperature, while it remains almost constant for $DyCuTe_2$ till 400°C and increases at higher temperatures. For all the phases, the Seebeck coefficient is positive, indicating that dominant carriers are holes.

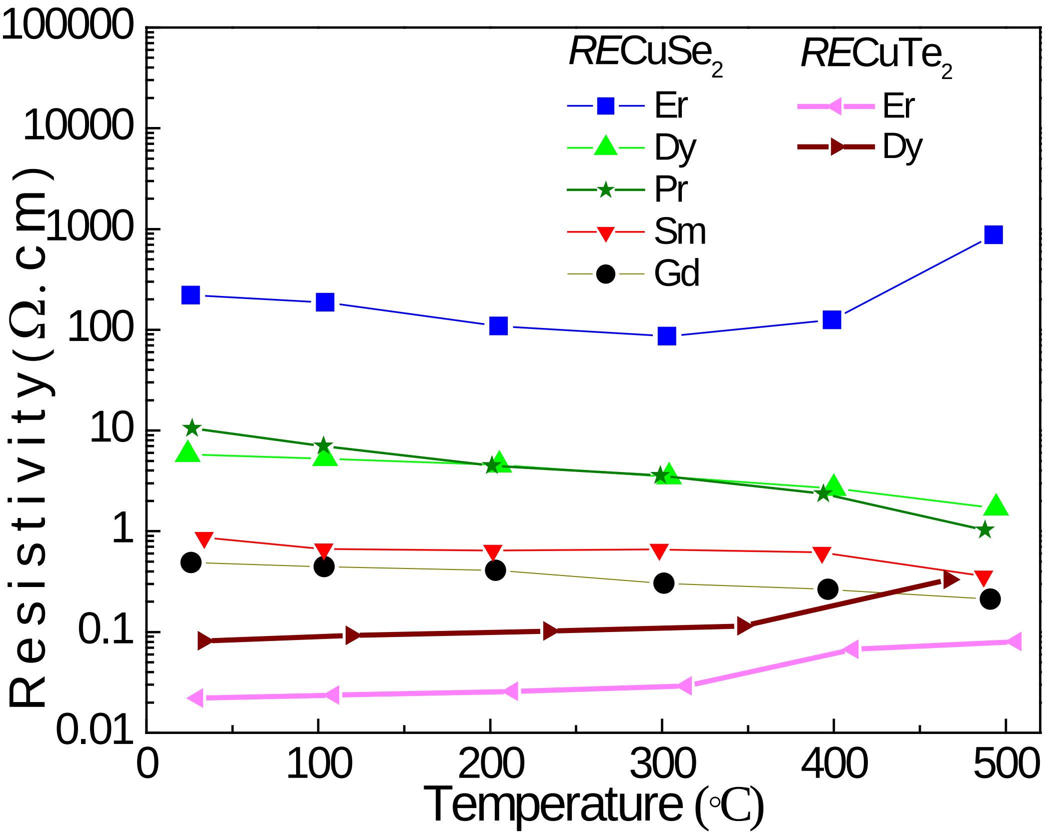

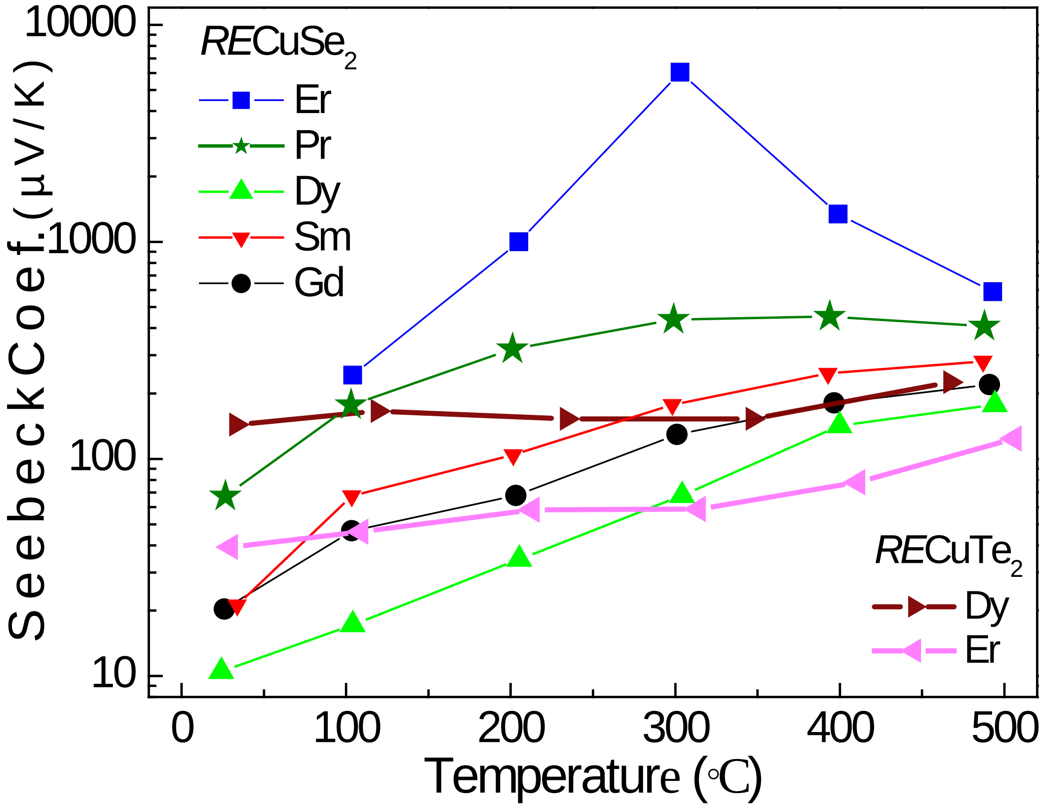

Figure 15. Electrical resistivity and the Seebeck coefficient for *RE*CuSe$_2$ (*RE*= Er, Dy, Gd, Pr and Sm) in contrast with *RE*CuTe$_2$ (*RE*= Er and Dy).

Table 8. Electrical resistivity and Seebeck coefficient at room temperature and activation energy of *RE*CuSe$_2$ (*RE*= Er, Dy, Gd, Pr and Sm) in contrast with *RE*CuTe$_2$ (*RE*= Er and Dy).

	$ErCuSe_2$	$DyCuSe_2$	$GdCuSe_2$	$PrCuSe_2$	$SmCuSe_2$	$DyCuTe_2$	$ErCuTe_2$
Resistivity at RT (Ω cm)	220	5.8	0.49	11	0.87	0.08	0.02
Activation Energy (eV)	0.11	0.05	0.04	0.12	-	-	-
Seebeck Coefficient at RT (μV/K)	233	11	20	67	21	144	39

5. Conclusion and future work

We have successfully synthesized a series of pure *RE*CuSe$_2$ (with *RE* = Pr, Sm, Gd, Dy and Er) and *RE*CuTe$_2$ (with *RE* = Er, Dy and Gd). The *RE*CuSe$_2$ phases adopt two structures, monoclinic and trigonal. The monoclinic structure offers larger coordination spheres for the *RE* atoms, and is stable for earlier *RE* atoms (Pr, Sm and Gd), while the trigonal one has a tighter *RE* environments, and is observed for the smaller *RE* atoms (Dy, Er). The trigonal phases contain the Cu site that is 50% occupied. While such deficiencies can be beneficial for the thermal conductivity, the electrical resistivity of the trigonal phases as well as the monoclinic one is too high for any thermoelectric applications.

The synthesized *RE*CuTe$_2$ phases (*RE* = Er, Dy and Gd) adopt a monoclinic structure, which feature disordered Cu sites. While such disorder may be beneficial for lowering their thermal conductivity, large values of electrical resistivity make these phases unsuitable for practical applications. When compared to corresponding selenides, the tellurides have lower resistivities, which stems from the closure of band gaps in their electronic structures. Structurally the *RE*CuTe$_2$ phases with *RE* = Er, Dy and Gd are similar to *RE*CuSe$_2$ with the $P\bar{3}m1$ structure. The monoclinic distortion in *RE*CuTe$_2$ is driven by Cu displacement inside larger tetrahedral voids in the hexagonal close packing of the Te atoms. Most likely, Cu shifts to one side of the Te tetrahedra optimize the Cu-Te interactions.

The optimization of the thermoelectric properties of the *RE*$CuSe_2$ phases may precede through doping the *RE* sites with alkaline-earth metals (e.g. Ca). Partial/complete replacement of Te in the Te-containing samples is another possible way to change the charge carrier concentration and to turn the metallic-type tellurides into semiconducting phases.

6. References

1. C. Kittel, Introduction to Solid State Physics, 7th ed., John Wiley & Sons, Inc., New York City, NY, (1996).
2. D.M. Rowe, Thermoelectrics Handbook; Macro to Nano, CRC Press, (2006).
3. G. M. Snyder, E. S. Toberer, Nature, Materials, 7 (2008) 105-114.
4. G. S. Nolas, D. T. Morelli, T. M. Tritt, Annu. Rev. Mat. Science, 29 (1999) 89.
5. G. S. Nolas, J. Poon, M. G. Kanatzidis, Mat. Res. Bull. 31 (2006) 199.
6. B. B. Iversen, A. E. C. Palmqvist, D. E. Cox, G. S. Nolas, G. D. Stucky, N. P.; Blake, H., J. Metiu, Solid State Chem., 149 (2000) 455-458.
7. D.-Y. Chung, T. Hogan, P. Brazis, M. Rocci-Lane, C. Kannewurf, M. Bastea, C. Uher, M. G. Kanatzidis, Science, 287 (2000) 1024.
8. D.-Y. Chung, T. P. Hogan, M. Rocci-Lane, P. Brazis, J. R. Ireland, C. R. Kannewurf, M. Bastea, C. Uher, M. G. Kanatzidis, J. Am. Chem. Soc., 126 (2004) 6414.
9. H. Liu, X. Shi, F. Xu, L. Zhang, W. Zhang, L. Chen, Q. Li, C. Uher, T. Day, G.J. Snyder, Nature, Materials, 11 (2012) 422-425.
10. B.A. Hunter, C.J. Howard, Rietica, Australian Nuclear Science and Technology, Menai, Australia, (2000).
11. M. Daszkiewicz, L.D. Gulay, V.Y. Shemet, A. Pietraszko, Z. Anorg. All. Chem., 634 (2008) 1201-1204.
12. STOE; STOE & Cie GmbH: Darmstadt, Germany; (2004).
13. G. M. Sheldrick, T. R. Schneider, Methods Enzymol., 277 (1997) 319−43.
14. O. K. Andersen, Z. Pawlowska, O. Jepsen, Phys. Rev. B, Condens Matter Mater. Phys., 34 (1986) 5253–69.
15. M. Julien-Pouzol, S. Jaulmes, A. Mazurier, M. Guittard, Acta Crystallogr. B: Struct. Crystallogr. Cryst. Chem., B37 (10) (1981)1901-3.

16. J.P. Dismukes, R.T. Smith, J.G. White, J. Phys. Chem. Solids, 32 (1971) 913-922.

17. L. Pauling, the Nature of the Chemical Bond, 2nd Ed., Cornell University Press: Ithaca, NY, (1948).

18. K.D. Machado, J.C. de Lima, T.A. Grandi, C.E.M. Campos, C.E. Maurmann, A.A.M. Gasperin, S.M. Souza, A.F. Pimenta, Acta Crystallogr. B, 60 (2004) 282-286.

19. M. Folchnandt, C. Schneck, T. Schleid, Z. Anorg. All. Chem., 630 (2004) 149-155.

20. M. Guittard, A. Benacerrat, J. Flahaut, Annal. Chim., 9 (1964) 25-34.

21. L.D. Gulay, I.D. Olekseyuk, A. Pietraszko, J. All. Comp., 403 (2005) 223-227.

22. I. Zulfugarl'i, R.S. Gamidov, A.B. Agaev, Azerb. Khim. Zhur., 1976, 5 (1976) 113-116.

23. F.-Q. Huang, P. Brazis, C.R. Kannewurf, J.A. Ibers, J. Am. Chem. Soc., 122 (2000), 80-86.

24. J. Flahaut, P. Laruelle, M.P. Pardo, M. Guittard, Bul. Soc. Chim. France, (1965) 1399-1404.

25. P.S. Herle, J.D. Corbett, Inorg. Chem., 40 (2001) 1858-1864.

26. L.H. Brixner, J. Inorg. Nucl. Chem., 15 (1960) 199-201.

27. R. Blachnik, M. Lasocka, U. Walbrecht, J. Solid State Chem., 48 (1983) 431-438.

28. R.V. Baranova, A.S. Avilov, Z.G. Pinsker, Kristallografiya, 18 (1973) 1169-1176.

29. L.D. Gulay, M. Daszkiewicz, V.Ya. Shemet, J. Solid State Chem., 186, 2 (2012) 142-148.

30. P.K. Mehrotra, R. Hoffmann, Inorg. Chem., 17, 8 (1978) 2187-2189.

31. F. Q. Huang, J. A. Ibers, Inorg. Chem., 38 (1999) 5978-5983.

32. J. R. Sootsman, D. Y. Chung, M. Kanatzidis, Angew. Chem. Int. Ed., 48 (2009) 8616-8639.

33. L.D. Gulay, I.D. Olekseyuk, M. Wolcyrz, J. Stepien-Damm, A. Pietraszko, J. All. Comp., 416 (2006) 173-178.

34. I. Ijjaali, K. Mitchell, J.A. Ibers, J. Solid State Chem., 177 (2004) 760- 764.

35. F.Q. Huang, J.A. Ibers, Inorg. Chem., 38 (1999) 5978-5983.

36. P.M. Julien-Pouzol, M. Guittard, Ann. Chim., 7 (1972) 253.

37. P.M. Julien-Pouzol, M. Guittard, J. Flahaut, Bull. Soc. Chim. France, 2 (1968) 533.

38. D.-Y. Chung, T. Hogan, M. Rocci-Lane, P. Brazis, J.R. Ireland, C.R. Kannewurf, M. Bastea, C. Uher, M. G. Kanatzidis, J. Am. Chem. Soc., 126, 20 (2004) 6414.

39. E.M. Godzhaev, O.M. Aliev, V.A. Mamedov, M.M. Zarbaliev, Neorg. Mater., 13 (1977) 441-443.

40. O.V. Marchuk, M. Daszkiewicz, L.D. Gulay, I.D. Olekseyuk, A. Pietraszko, J. All. Comp., 455 (2008) 186-190.

41. Mehdi Esmaeili, Yu-Chi Tseng, Yurij Mozharivskyj, Journal of Alloys and Compounds, 610 (2014) 555-560.

42. Mehdi Esmaeili, Scott Forbes, Yu-Chi Tseng, Yurij Mozharivskyj, Journal of Solid State Sciences, 36 (2014) 89-93.